Song He
Acoustics and Dynamics Laboratory,
Department of Mechanical Engineering,
The Ohio State University,
Columbus, OH 43210
e-mail: he.81@osu.edu

Rajendra Gunda
Advanced Numerical Solutions,
Hilliard, OH 43026
e-mail: gunda.2@osu.edu

Rajendra Singh[1]
ASME Fellow
Acoustics and Dynamics Laboratory,
Department of Mechanical Engineering and The
Center for Automotive Research,
The Ohio State University,
Columbus, OH 43210
e-mail: singh.3@osu.edu

Inclusion of Sliding Friction in Contact Dynamics Model for Helical Gears

This paper proposes a new analytical model for helical gears that characterizes the contact plane dynamics and captures the velocity reversal at the pitch line due to sliding friction. First, the tooth stiffness density function along the contact lines is calculated by using a finite element code. Analytical formulations are then derived for the multidimensional mesh forces and moments. Contact zones for multiple tooth pairs in contact are identified, and the associated integration algorithms are derived. A new 12-degree-of-freedom, linear time-varying model with sliding friction is then developed. It includes rotational and translational motions along the line-of-action, off-line-of-action, and axial directions. The methodology is also illustrated by predicting time and frequency domain results for several values of the coefficient of friction. [DOI: 10.1115/1.2359474]

1 Introduction

Sliding friction is believed to be one of the major sources of gear vibration and noise especially under high-torque and low-speed conditions since a reversal in the sliding velocity takes place along the pitch line. Yet few analytical contact dynamics formulations that incorporate friction are available in the literature [1–9]. In a series of recent papers, Vaishya and Singh [1–3] reviewed various modeling strategies that have been historically adopted and then illustrated issues for spur gears by assuming equal load sharing among the contact teeth. Furthermore, Velex and Cahouet [4] considered the effects of sliding friction in their models for spur and helical gears. They found that the dynamic bearing forces, as caused by friction at lower speeds, can generate significant time-varying excitations. Velex and Sainsot [5] examined friction excitations in errorless spur and helical gear pairs, and reported that the friction appears as a non-negligible excitation source, especially for translating motions. Lundvall et al. [6] proposed a multibody model for spur gears and briefly discussed the role of profile modification in the presence of sliding friction. He et al. [7] have developed a more accurate model of the spur gears, which includes realistic mesh stiffness and sliding friction, while overcoming the deficiency of Vaishya and Singh's work [1–3]. In particular, this model shows that the tip relief could even amplify dynamic motions in some cases due to interactions between mesh and friction forces. Based on the literature review, it is clear that sliding friction has not been adequately considered in the dynamic models for helical gears. This paper attempts to fill this void.

2 Problem Formulation

In a helical gear pair, the line-of-action (LOA) lies in the tangent plane of the base cylinders, as defined by the base helix angle β_b. Consequently, the moment arms for the out-of-plane moments change constantly. This phenomenon introduces axial and friction force shuttling effects [4]. Thus, the friction forces play a pivotal role in the loads transmitted to the bearings, especially in the off-line-of-action (OLOA) direction. Blankenship and Singh [10] have developed a three-dimensional representation of forces and moments generated and transmitted via a gear mesh interface. This model is formulated in terms of the spatially varying mesh stiffness and transmission errors, which are assumed to be available from quasi-static elastic analyses. The vector formulation leads to a multibody analysis of geared systems, and force coupling due to vibratory changes in the contact plane is directly included. Similar strategy will be adopted here.

The objectives of this paper include the following. First, propose a three-dimensional formulation to characterize the dynamics associated with the contact plane, including the reversal at the pitch line due to sliding friction. Calculation of the contact forces/moments will be illustrated via an example case (NASA-ART helical gear pair). The tooth stiffness density along contact lines will then be calculated using a finite element/contact mechanics (FE/CM) analysis code [11]. Second, develop a multi-degree-of-freedom (MDOF) helical gear pair model (with 12 DOFs), which includes the rotational and translational DOFs along the LOA, OLOA, and axial directions as well as the bearing/shaft compliances. Third, illustrate the effect of sliding friction, including the shuttling effect in the radial direction and coupling between the LOA and OLOA directions. The following assumptions are made to derive the MDOF linear time-varying system (LTV) model:

1. The position of the contact lines and relative sliding velocity depend only on the mean angular motions of the gear pair. If this assumption is not made, the system will have implicit non-linearities.
2. The mesh stiffness per unit length along the contact line (or stiffness density k) is constant [8]. The constant k is estimated from the geometrical calculation of total length of contact lines and the mesh stiffness, which is computed using the finite element model [11]; this is equivalent to the equal load sharing assumption in spur gears [1–3].
3. Coulomb's law with a constant coefficient of friction (μ) is employed similar to previous researchers [1–3,7], though mixed lubrication regime exists.
4. The elastic deformations of the shaft and bearings are modeled using lumped parameter representations for their compliances. Also, it is assumed that the mean load is high and the dynamic load is not sufficient to cause tooth separations [12]. Thus vibroimpacts are not considered here.

[1]Corresponding author

Contributed by the Power Transmission and Gearing Committee of ASME for publication in the JOURNAL OF MECHANICAL DESIGN. Manuscript received December 26, 2005; final manuscript received April 29, 2006. Review conducted by David Dooner.

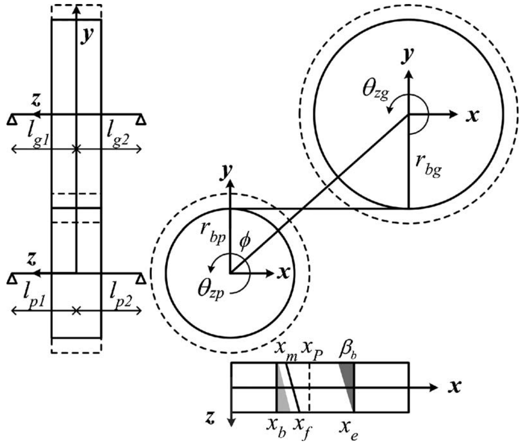

Fig. 1 Schematic of the helical gear pair system

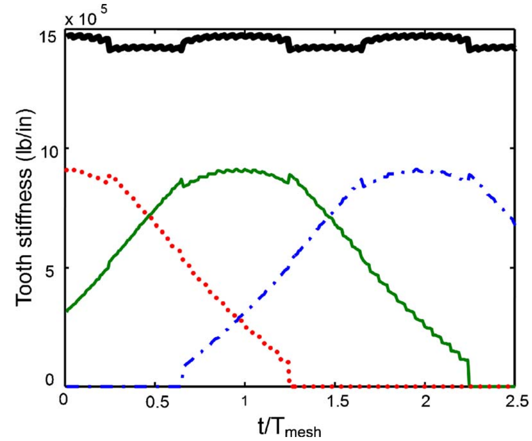

Fig. 2 Tooth stiffness function calculated using Eq. (1) based on the FE/CM code [11]. Key: red dotted line, tooth pair 0; green solid line, tooth pair 1; blue dashed-dotted line, tooth pair 2; thick solid line, combined tooth pair stiffness.

3 Mesh Forces and Moments With Sliding Friction

The helical gear system is depicted in Fig. 1. The pinion and gear are modeled as rigid cylinders linked by a series of independent stiffness elements that describe the contact plane tangent to the base cylinders. The normal direction at a point of contact lies in the contact plane (due to the involute profile construction) and is perpendicular to the line of contact. The pinion and gear dynamics are formulated in the coordinate systems located at their respective centers, as shown in Fig. 1. The nominal motions of the pinion and gear are given as $-\Omega_p e_z$ and $\Omega_g e_z = e_z \Omega_p r_{bp}/r_{bg}$, respectively. Here, z axis coincides with the axial direction, e is the unit directional vector, and r_{bp} and r_{bg} are the base radii of pinion and gear. An (static) input torque T_p is applied to the pinion, and the (static) braking torque T_g on the gear obeys the basic gear kinematics. Superposed on the kinematic motions are rotational vibratory motions denoted by θ_{zp} and θ_{zg} for the pinion and gear. For the sake of illustration, analytical formulations are demonstrated via the following example case with parameters of the pinion (gear parameters are within the parenthesis): number of teeth 25 (31); outside diameter 3.38 (4.13) in.; pitch diameter 3.125 (3.875) in.; root diameter 2.811 (3.561) in.; center distance 3.5 in.; transverse diametral pitch 8 in.$^{-1}$; transverse pressure angle 25 deg; helix angle 21.5 deg; face width 1.25 in.; polar moment of inertia 8.33×10^{-3} (1.64×10^{-2}) lb s^2 in.; mass 1.26×10^{-2} (1.58×10^{-2}) lb s^2/in. Since the overall contact ratio is $\sim$2.7, either two or three tooth pairs are meshing with each other at any time instant. The three meshing tooth pairs within a mesh cycle are numbered as 0, 1, and 2, respectively. Calculate the (static) contact loads $N_0(t)$, $N_1(t)$, $N_2(t)$, and (static) pinion deflection $\Theta_{zp}(t)$ by performing a static analysis using the FE/CM formulation [11]. The stiffnesses $K_0(t)$, $K_1(t)$, and $K_2(t)$ of the three meshing tooth pairs are calculated as follows:

$$K_i(t) = \frac{N_i(t)}{r_{bp}\Theta_{zp}(t)}, \quad i = 0,1,2 \tag{1}$$

For our example, the single tooth-pair stiffness function $K(t)$ is obtained by following one tooth pair for three complete mesh cycles, as shown in Fig. 2, where T_{mesh} is the period of one mesh cycle. Observe that the stiffness profile has a trapezoidal shape; some discontinuities exist where corner contacts take place. The overall stiffness function, defined as a combination of all meshing tooth pairs, also follows a trapezoidal pattern. Meanwhile, the sum of the lengths of contact lines can be calculated by using either the FE/CM code [11,13] or a simplified approximation method based on gear geometry [14]. Since the total length of contact lines and combined tooth stiffness follow a similar pattern, we can assume a constant mesh stiffness density (k) along the contact lines. Consequently, the time-averaged k is estimated as follows, where L_i is the length of the ith contact line,

$$k \approx \sum_{i=0}^{2} K_i(t) \bigg/ \sum_{i=0}^{2} L_i \tag{2}$$

Denote the LOA, OLOA, and axial axes as x-, y-, and z-axes, respectively; the dynamic motions of the pinion and gear centers consist of three translations (u) and three rotations (θ) such that $u_p=\{u_{xp}, u_{yp}, u_{zp}, \theta_{xp}, \theta_{yp}, \theta_{zp}\}^T$, $u_g=\{u_{xg}, u_{yg}, u_{zg}, \theta_{xg}, \theta_{yg}, \theta_{zg}\}^T$. For a contact point with local coordinates (x, r_{bp}, z) in the pinion coordinate system, its global motion when considered as part of the pinion is derived as

$$u_{pc} = \begin{Bmatrix} u_{xp} \\ u_{yp} \\ u_{zp} \end{Bmatrix} + \begin{Bmatrix} \theta_{xp} \\ \theta_{yp} \\ \theta_{zp} \end{Bmatrix} \times (xe_x + r_{bp}e_y + ze_z) = \begin{Bmatrix} u_{xp} + z\theta_{yp} + r_{bp}\Omega_p t - r_{bp}\theta_{zp} \\ u_{yp} - z\theta_{xp} - x\Omega_p t + x\theta_{zp} \\ u_{zp} + r_{bp}\theta_{xp} - x\theta_{yp} \end{Bmatrix} \tag{3a}$$

Denote x_g as the x coordinate at the gear center in the pinion coordinate system, the global motion of the contact point when it is considered as part of the gear is

$$u_{gc} = \begin{Bmatrix} u_{xg} \\ u_{yg} \\ u_{zg} \end{Bmatrix} + \begin{Bmatrix} \theta_{xg} \\ \theta_{yg} \\ \theta_{zg} \end{Bmatrix} \times [-(x_g - x)e_x - r_{bg}e_y + ze_z] = \begin{Bmatrix} u_{xg} + z\theta_{yg} + r_{bg}\Omega_g t + r_{bg}\theta_{zg} \\ u_{yg} - z\theta_{xg} - (x_g - x)\Omega_g t - (x_g - x)\theta_{zp} \\ u_{zg} - r_{bg}\theta_{xg} + (x_g - x)\theta_{yg} \end{Bmatrix} \tag{3b}$$

The deformation of the mesh spring is $\Delta_{\text{mesh}}=(u_{pc}-u_{gc})\cdot(-\cos\beta_b e_x + \sin\beta_b e_z)$, which can be further simplified as

$$\begin{aligned} \Delta_{\text{mesh}} = &-\cos\beta_b[(u_{xp} - u_{xg}) + z(\theta_{yp} - \theta_{yg}) - (r_{bp}\theta_{zp} + r_{bg}\theta_{zg})] \\ &+ \sin\beta_b[(u_{zp} - u_{zg}) + (r_{bp}\theta_{xp} + r_{bg}\theta_{xg}) \\ &- (x\theta_{yp} + (x_g - x)\theta_{yg})] \end{aligned} \tag{4}$$

The velocities of the contact point when considered as part of the pinion or gear (ignoring the vibratory component) are derived as

$$v_{pc} = r_{bp}\Omega_p e_x - x\Omega_p e_y, \tag{5a}$$

$$v_{gc} = r_{bg}\Omega_g e_x - (x_g - x)\Omega_g e_y \tag{5b}$$

The relative sliding velocity of the pinion with respect to the gear is

$$v_s = [-x\Omega_p + (x_g - x)\Omega_g]e_y \tag{6}$$

From Eq. (6), it is clear that v_s is in the positive y direction at the beginning of contact (small x). Furthermore, v_s becomes zero at the pitch point x_P and changes to the negative y direction when $x > x_P$. Hence, Eq. (6) can be used to determine the direction of the friction forces. The elemental forces on the meshing tooth pairs of the pinion and the gear are given in Eq. (7) assuming only the elastic effects, and the total mesh forces are derived by integrating the elemental forces over the contact line as given in Eq. (8),

$$\Delta F_{\text{mesh},p} = -\Delta F_{\text{mesh},g} = \begin{Bmatrix} -k\Delta_{\text{mesh}}\cos\beta_b \\ \mu k\Delta_{\text{mesh}}\,\text{sgn}(x - x_P) \\ k\Delta_{\text{mesh}}\sin\beta_b \end{Bmatrix} \tag{7}$$

$$F_{\text{mesh},p} = -F_{\text{mesh},g} = \begin{Bmatrix} -k\cos\beta_b \displaystyle\int_l \Delta_{\text{mesh}} dl \\ \mu k \displaystyle\int_l \Delta_{\text{mesh}}\,\text{sgn}(x - x_P) dl \\ k\sin\beta_b \displaystyle\int_l \Delta_{\text{mesh}} dl \end{Bmatrix} \tag{8}$$

To facilitate the integration, the contact zone is divided into three regions, as shown in Fig. 1, where x_b and x_e are defined as the lower and upper boundaries of the contact zone in the LOA coordinate system of the pinion. In region 1 (lightly shaded area within the contact zone of Fig. 1), the lower and upper limits of x are denoted as $x_m = x_b$ and $x_f \geqslant x_b$, respectively. The z coordinate (on the line of contact) is written as a function of the x coordinate as follows, where W is the face width,

$$z(x) = 0.5W + \frac{x - x_f}{\tan\beta_b} \tag{9a}$$

In region 2 (white area within the contact zone of Fig. 1), $x_m \geqslant x_b$ and $x_f \leqslant x_e$. The z coordinate of the contact point is derived as

$$z(x) = \frac{0.5W(2x - x_f - x_m)}{x_f - x_m} \tag{9b}$$

In region 3 (darkly shaded area within the contact zone of Fig. 1), $x_m \leqslant x_e$ and $x_f = x_e$. The z coordinate of a contact point is given as

$$z(x) = -0.5W + \left[\frac{x - x_m}{\tan\beta_b}\right] \tag{9c}$$

Consider the integral in Eq. (8),

$$\begin{aligned}\bar{\Delta} = \int_l \Delta_{\text{mesh}} dl = \int_l (&-\cos\beta_b[(u_{xp} - u_{xg}) + z(\theta_{yp} - \theta_{yg}) \\ &- (r_{bp}\theta_{zp} + r_{bg}\theta_{zg})] + \sin\beta_b\{(u_{zp} - u_{zg}) + (r_{bp}\theta_{xp} \\ &+ r_{bg}\theta_{xg}) - [x\theta_{yp} + (x_e - x)\theta_{yg}]\})dl \end{aligned} \tag{10a}$$

Recognizing that $dz = dl\cos\beta_b$ and $dx = dl\sin\beta_b$, the above integral yields

$$\begin{aligned}\bar{\Delta} = &-(z_f - z_m)[(u_{xp} - u_{xg}) - (r_{bp}\theta_{zp} + r_{bg}\theta_{zg})] - 0.5(z_f^2 - z_m^2) \\ &\cdot(\theta_{yp} - \theta_{yg}) + (x_f - x_m)[(u_{zp} - u_{zg}) + (r_{bp}\theta_{xp} + r_{bg}\theta_{xg}) - x_e\theta_{yg}] \\ &- 0.5(x_f^2 - x_m^2)(\theta_{yp} - \theta_{yg}) \end{aligned} \tag{10b}$$

Compare Eqs. (8) and (10) and represent the contact forces in the LOA and axial directions on the pinion as:

$$F_{\text{mesh},p,x} = -k\cos\beta_b\bar{\Delta}, \tag{11a}$$

$$F_{\text{mesh},p,z} = k\sin\beta_b\bar{\Delta} \tag{11b}$$

Because of the sliding friction, the $F_{\text{mesh},p,y}$ involves a discontinuous sign function and it needs to be evaluated separately for three different cases assuming a constant μ. *Case 1*. Both limits of the contact line are less than x_P, which implies the contact line on the pinion is completely below the pitch cylinder (approach action) so that $\text{sgn}(x - x_P) = -1$. The friction force of the pinion is

$$F_{\text{mesh},p,y} = -\mu k\bar{\Delta} \tag{12}$$

Case 2. The contact line lies on either side of the pitch cylinder. The integral of friction force need to be evaluated in two parts

$$F_{\text{mesh},p,y} = \mu k(\bar{\Delta}_2 - \bar{\Delta}_1) \tag{13a}$$

$$\begin{aligned}\bar{\Delta}_1 = &-(z_P - z_m)[(u_{xp} - u_{xg}) - (r_{bp}\theta_{zp} + r_{bg}\theta_{zg})] - 0.5(z_P^2 - z_m^2) \\ &\cdot(\theta_{yp} - \theta_{yg}) + (x_P - x_m)[(u_{zp} - u_{zg}) + (r_{bp}\theta_{xp} + r_{bg}\theta_{xg}) \\ &- x_e\theta_{yg}] - 0.5(x_P^2 - x_m^2)(\theta_{yp} - \theta_{yg}) \end{aligned} \tag{13b}$$

$$\begin{aligned}\bar{\Delta}_2 = &-(z_f - z_P)[(u_{xp} - u_{xg}) - (r_{bp}\theta_{zp} + r_{bg}\theta_{zg})] - 0.5(z_f^2 - z_P^2) \\ &\cdot(\theta_{yp} - \theta_{yg}) + (x_f - x_P)[(u_{zp} - u_{zg}) + (r_{bp}\theta_{xp} + r_{bg}\theta_{xg}) - x_e\theta_{yg}] \\ &- 0.5(x_f^2 - x_P^2)(\theta_{yp} - \theta_{yg}) \end{aligned} \tag{13c}$$

Case 3. Both limits are greater than x_P, which implies the contact line on the pinion is completely above the pitch cylinder (recess action). Consequently, $\text{sgn}(x - x_P) = 1$ and the friction force on the pinion is

$$F_{\text{mesh},p,y} = \mu k\bar{\Delta} \tag{14}$$

Hence, in summary the mesh forces are derived as

$$F_{\text{mesh},p} = -F_{\text{mesh},g} = \begin{Bmatrix} -k\cos\beta_b\bar{\Delta} \\ -\mu k\bar{\Delta} \text{ or } \mu k(\bar{\Delta}_2 - \bar{\Delta}_1) \text{ or } \mu k\bar{\Delta} \\ k\sin\beta_b\bar{\Delta} \end{Bmatrix} \tag{15}$$

The elemental moments on the pinion at a point on the contact line are derived as

$$\Delta M_{\text{mesh},p} = k\Delta_{\text{mesh}} \begin{Bmatrix} r_{bp}\sin\beta_b - z\mu\,\text{sgn}(x - x_P) \\ -x\sin\beta_b - z\cos\beta_b \\ x\mu\,\text{sgn}(x - x_P) + r_{bp}\cos\beta_b \end{Bmatrix} \tag{16}$$

Integrating Eq. (16) over the contact line yields the total moments on the pinion as

$$M_{\text{mesh},p} = \int_l \Delta M_{\text{mesh},p} dl \tag{17}$$

To facilitate the calculation of Eq. (17), define two integration operations over the line of contact with lower and higher limits x_l and x_h, respectively,

$$\begin{aligned}(\Delta\cdot x)(x_l, x_h) = \int_{x_l}^{x_h} x\Delta_{\text{mesh}} dl = &-\frac{(x_h + x_l)(z_h - z_l)}{2}(c_1 + c_2 z_f) \\ &+ \frac{x_h^2 - x_l^2}{2}c_3 - \frac{x_h^3 - x_l^3}{3}c_2 - (z_h - z_f)^2 \\ &\cdot\left(\frac{x_h - x_f}{3} + \frac{x_f}{2}\right)c_2 + (z_l - z_f)^2 \end{aligned}$$

$$\cdot\left(\frac{x_l - x_f}{3} + \frac{x_f}{2}\right)c_2 \tag{18a}$$

$$(\Delta\cdot z)(x_l,x_h) = \int_{x_l}^{x_h} z\Delta_{\text{mesh}}dl = (-c_1 + c_3\tan\beta_b)\frac{z_h^2 - z_l^2}{2} - c_2\frac{z_h^3 - z_l^3}{3} - c_2\frac{x_f\tan\beta_b}{2}(z_h^2 - z_l^2) - c_2\tan^2\beta_b \cdot\left(\frac{z_h^3 - z_l^3}{3} - \frac{z_f(z_h^2 - z_l^2)}{2}\right) \tag{18b}$$

$$c_1 = (u_{xp} - u_{xg}) - (r_{bp}\theta_{zp} + r_{bg}\theta_{zg}) \tag{18c}$$

$$c_2 = (\theta_{yp} - \theta_{yg}) \tag{18d}$$

$$c_3 = (u_{zp} - u_{zg}) + (r_{bp}\theta_{xp} + r_{bg}\theta_{xg}) - x_e\theta_{yg} \tag{18e}$$

Common integrals in the vector Eq. (17) are now evaluated as follows:

$$\int_l x\Delta_{\text{mesh}}dl = (\Delta\cdot x)(x_m,x_f) \tag{19a}$$

$$\int_l z\Delta_{\text{mesh}}dl = (\Delta\cdot z)(x_m,x_f) \tag{19b}$$

$$\int_l x\,\text{sgn}(x - x_P)\Delta_{\text{mesh}}dl = -(\Delta\cdot x)(x_m,x_P) + (\Delta\cdot x)(x_P,x_f) \tag{19c}$$

$$\int_l z\,\text{sgn}(x - x_P)\Delta_{\text{mesh}}dl = -(\Delta\cdot z)(x_m,x_P) + (\Delta\cdot z)(x_P,x_f) \tag{19d}$$

Consequently, the moments of the mesh force acting on the pinion are given as

$$M_{\text{mesh},p} = k\begin{Bmatrix} r_{bp}\bar{\Delta}\sin\beta_b + \mu(\Delta\cdot z)(x_m,x_P) - \mu(\Delta\cdot z)(x_P,x_f) \\ -\sin\beta_b(\Delta\cdot x)(x_m,x_f) - (\Delta\cdot z)(x_m,x_f)\cos\beta_b \\ -\mu(\Delta\cdot x)(x_m,x_P) + \mu(\Delta\cdot x)(x_P,x_f) + r_{bp}\bar{\Delta}\cos\beta_b \end{Bmatrix} \tag{20}$$

Similarly, the moments of the elemental mesh forces on the gear are given as

$$\Delta M_{\text{mesh},g} = k\Delta_{\text{mesh}}\begin{Bmatrix} r_{bg}\sin\beta_b + z\mu\,\text{sgn}(x - x_P) \\ -x_e\sin\beta_b + x\sin\beta_b + z\cos\beta_b \\ x_g\mu\,\text{sgn}(x - x_P) - x\mu\,\text{sgn}(x - x_P) + r_{bg}\cos\beta_b \end{Bmatrix} \tag{21}$$

The total moments due to the mesh forces on the gear are derived as

$$M_{\text{mesh},g} = k\begin{Bmatrix} r_{bg}\bar{\Delta}\sin\beta_b - \mu(\Delta\cdot z)(x_m,x_P) + \mu(\Delta\cdot z)(x_P,x_f) \\ -x_g\bar{\Delta}\sin\beta_b + \sin\beta_b(\Delta\cdot x)(x_m,x_f) + (\Delta\cdot z)(x_m,x_f)\cos\beta_b \\ x_g(\bar{\Delta}_2 - \bar{\Delta}_1) + \mu(\Delta\cdot x)(x_m,x_P) - \mu(\Delta\cdot x)(x_P,x_f) + r_{bg}\bar{\Delta}\cos\beta_b \end{Bmatrix} \tag{22}$$

Note that Eqs. (15), (20), and (22) are formulated for a single tooth pair in contact. For multiple tooth pairs in contact, the dynamics of all meshing tooth pair must be considered. Consider an example to demonstrate the modeling strategy. Since the contact ratio is ~2.7, three tooth pairs are considered in a single mesh cycle. For a generic helical gear pair with contact ratio σ, n =ceil(σ) number of meshing tooth pairs need to be considered by following the same methodology, where the "ceil" function rounds σ to the nearest integers toward infinity. Figure 3(*a*) shows the contact plan of the example case within a helical gear pair and Fig. 3(*b*) illustrates a zoomed-in snapshot of the contact zone at the beginning of a mesh cycle. At this instant, pair 0 just comes into mesh at point A and pair 1 is in contact along line CI. Likewise pair 2 contacts each other along line MN. As the gears roll, the contact lines move diagonally across the contact zone. When pair 0 reaches the pitch point P, the relative sliding velocity of the pinion with respect to the gear starts to reverse, resulting in a reversal of friction force along the portion of contact line surpass the pitch point. Once pair 0 reaches the CI line (and pair 1 reaches MN line) at the end of the mesh circle, pair 0 becomes pair 1 (and pair 1 becomes pair 2) corresponding to the start of the next mesh cycle. At any time instant t, the x coordinates of the three pairs are projected along the AR line and denoted as $x_0(t)$, $x_1(t)$, and $x_2(t)$, as defined below in Eq. (23). Here, λ is the base pitch, L represents the geometrical distance, and "mod" is the modulus function defined as $\text{mod}(x,y) = x - y\cdot\text{floor}(x/y)$, if $y \neq 0$.

$$x_0(t) = \text{mod}(\Omega_p r_{bp}t,\lambda) + L_{\text{T}_1\text{A}} \tag{23a}$$

$$x_1(t) = \text{mod}(\Omega_p r_{bp}t,\lambda) + \lambda + L_{\text{T}_1\text{A}} \tag{23b}$$

$$x_2(t) = \text{mod}(\Omega_p r_{bp}t,\lambda) + 2\lambda + L_{\text{T}_1\text{A}} \tag{23c}$$

To implement the integration algorithm, the contact regions are further divided into eight contact zones as shown in Fig. 3(*b*). Zones 1 and 2 correspond to pair 0 before and after reaching the pitch line; zones 3–5 and zones 6–8 correspond to pairs 1 and 2, respectively. The zone classifications and their corresponding integration limits for the calculation of dynamic forces and moments are derived as following, where x_m, x_f, z_m, and z_f denote the lower and upper limits along the x- and z-axes.

$$\text{Zone 1}(L_{\text{T}_1\text{A}} \leqslant x_0(t) < L_{\text{T}_1\text{P}}):\quad x_m = L_{\text{T}_1\text{A}},\quad x_f = x_0,$$
$$z_f = 0.5W,\quad z_m = 0.5W - \left[\frac{x_0 - L_{\text{T}_1\text{A}}}{\tan\beta_b}\right] \tag{24a}$$

$$\text{Zone 2}(L_{\text{T}_1\text{P}} \leqslant x_0(t) < L_{\text{T}_1\text{C}}):\quad x_m = L_{\text{T}_1\text{A}},\quad x_f = x_0,$$
$$x_p = L_{\text{T}_1\text{P}}, \tag{24b}$$
$$z_f = 0.5W,\quad z_m = 0.5W - \left[\frac{x_0 - L_{\text{T}_1\text{A}}}{\tan\beta_b}\right],\quad z_p = 0.5W - \left[\frac{x_0 - L_{\text{T}_1\text{P}}}{\tan\beta_b}\right]$$

$$\text{Zone 3}(L_{\text{T}_1\text{C}} \leqslant x_1(t) < L_{\text{T}_1\text{Q}}):\quad x_m = L_{\text{T}_1\text{A}},\quad x_f = x_1,$$

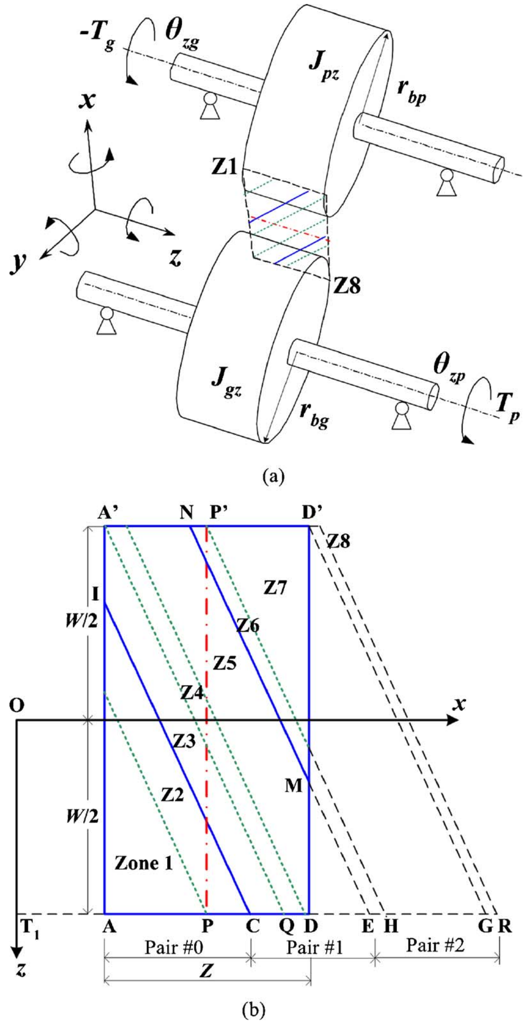

Fig. 3 Contact zones at the beginning of a mesh cycle: (*a*) in the helical gear pair and (*b*) contact zones within contact plane. Key: PP′ is the pitch line; AA′ is the face width *W*; AD is the length of contact zone *Z*.

$$x_p = L_{\mathrm{T_1P}}, \quad z_f = 0.5W, \quad z_m = 0.5W - \left[\frac{x_1 - L_{\mathrm{T_1A}}}{\tan \beta_b}\right], \tag{24c}$$

$$z_p = 0.5W - \left[\frac{x_1 - L_{\mathrm{T_1P}}}{\tan \beta_b}\right]$$

$$\text{Zone } 4(L_{\mathrm{T_1Q}} \leqslant x_1(t) < L_{\mathrm{T_1D}}): \quad x_m = x_1 - W \cdot \tan \beta_b,$$

$$x_f = x_1, \quad x_p = L_{\mathrm{T_1P}}, \quad z_m = -0.5W \quad z_f = 0.5W, \tag{24d}$$

$$z_p = 0.5W - \left[\frac{x_1 - L_{\mathrm{T_1P}}}{\tan \beta_b}\right]$$

$$\text{Zone } 5(L_{\mathrm{T_1D}} \leqslant x_1(t) < L_{\mathrm{T_1E}}): \quad x_m = x_1 - W \tan \beta_b,$$

$$x_f = L_{\mathrm{T_1D}}, \quad x_p = L_{\mathrm{T_1P}}, \quad z_m = -0.5W, \tag{24e}$$

$$z_f = 0.5W - \left[\frac{x_1 - L_{\mathrm{T_1D}}}{\tan \beta_b}\right], \quad z_p = 0.5W - \left[\frac{x_1 - L_{\mathrm{T_1P}}}{\tan \beta_b}\right]$$

$$\text{Zone } 6(L_{\mathrm{T_1E}} \leqslant x_2(t) < L_{\mathrm{T_1H}}): \quad x_m = x_2 - W \cdot \tan \beta_b,$$

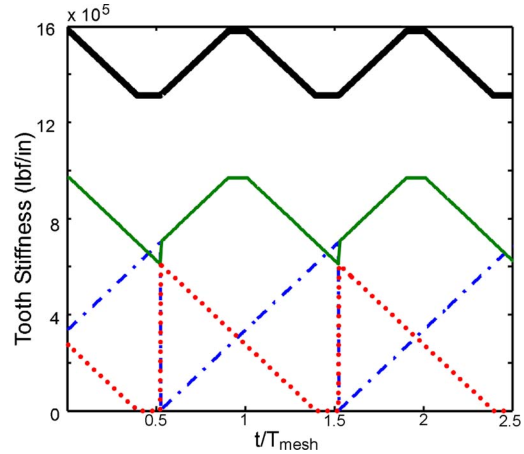

Fig. 4 Predicted tooth stiffness functions. Predicted tooth stiffness functions. Key: blue dashed-dotted line, tooth pair 0; green solid line, tooth pair 1; red dotted line, tooth pair 2; thick solid line, combined tooth pair stiffness.

$$x_f = L_{\mathrm{T_1D}}, \quad x_p = L_{\mathrm{T_1P}}, \quad z_m = -0.5W, \tag{24f}$$

$$z_f = 0.5W - \left[\frac{x_2 - L_{\mathrm{T_1D}}}{\tan \beta_b}\right], \quad z_p = 0.5W - \left[\frac{x_1 - L_{\mathrm{T_1P}}}{\tan \beta_b}\right]$$

$$\text{Zone } 7(L_{\mathrm{T_1H}} \leqslant x_2(t) < L_{\mathrm{T_1G}}): \quad x_m = x_2 - W \cdot \tan \beta_b,$$

$$x_f = L_{\mathrm{T_1D}}, \quad z_m = -0.5W, \quad z_f = 0.5W - \left[\frac{x_2 - L_{\mathrm{T_1D}}}{\tan \beta_b}\right] \tag{24g}$$

$$\text{Zone } 8(L_{\mathrm{T_1G}} \leqslant x_2(t) < L_{\mathrm{T_1R}}): \quad \text{No definition} \tag{24h}$$

Figure 4 shows the analytical tooth stiffness functions of each meshing tooth pair and the combined stiffness calculated for the example case by using the integration algorithm. Observe that both magnitude and shape of the stiffness functions in Fig. 4 correlate well with those in Fig. 2, which are obtained using a detailed FE/CM code [11]. Note that the stiffness functions in Fig. 4 are defined similar to Eq. (23), which is different from the definition of Eq. (1) corresponding to Fig. 2.

4 Shaft and Bearing Models

Consider the simplified shaft model of Fig. 5, where l_1 and l_2 are the distances between the pinion/gear center to the bearing springs, E is the Young's modulus, $I=\pi r_s^4/4$ is the area moment of inertia and A is the cross-sectional area [15,16]. The shaft stiffness matrix $[K]_S$ corresponding to the displacement vector $[x, y, z, \theta_x, \theta_y, \theta_z]^T$ is

$$[K]_S = \begin{bmatrix} K_{Sxx} & 0 & 0 & 0 & -K_{Sx\theta_y} & 0 \\ & K_{Syy} & 0 & K_{Sy\theta_x} & 0 & 0 \\ & & K_{Szz} & 0 & 0 & 0 \\ & & & K_{S\theta_x\theta_x} & 0 & 0 \\ & \text{sym.} & & & K_{S\theta_y\theta_y} & 0 \\ & & & & & 0 \end{bmatrix} \tag{25}$$

where $K_{Sxx}=K_{Syy}=3EI(l_1+l_2)[(l_1-l_2)^2+l_1l_2]/(l_1l_2)^3$ is the bending stiffness, $K_{S\theta_x\theta_x}=K_{S\theta_y\theta_y}=3EI(l_1+l_2)/(l_1l_2)$ is the rocking stiffness, $K_{Sx\theta_y}=K_{Sy\theta_x}=3EI(l_1^2-l_2^2)/(l_1l_2)^2$ is the rocking-bending coupled stiffness and $K_{Szz}=AE/(l_1+l_2)$ is the longitudinal stiffness. The rolling element bearings in Fig. 5 are modeled by a stiffness matrix $[K]_B$ of dimension six as proposed by Lim and

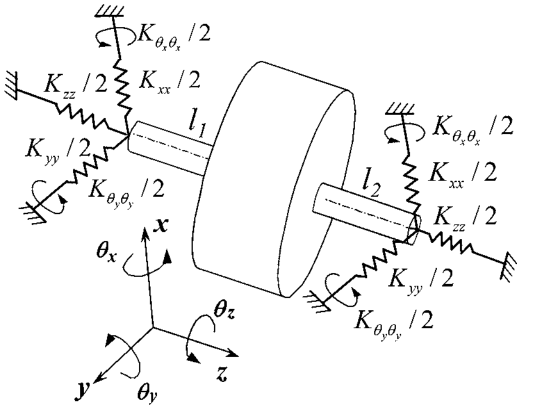

Fig. 5 Schematic of the bearing-shaft model. Here, the shaft and bearing stiffness elements are assumed to be in series to each other. Only pure rotational or translational stiffness elements are shown. Coupling stiffness terms $K_{x\theta_y}$, $K_{x\theta_x}$ are not shown.

Singh [17]. The mean shaft loads and bearing preloads are assumed constant to ensure a time-invariant $[K]_B$ matrix. Assume that each shaft is supported by two identical axially preloaded high-precision deep groove ball bearings with a mean axial displacement. The helical gear pair is driven by a mean load T_{m}, which also generates mean radial force F_{Bx} in the LOA direction, axial force F_{Bz} and moment M_{ym} around OLOA direction. The $[K]_B$ matrix for each bearing under mean loads has significant coefficients K_{Bxx}, K_{Byy}, K_{Bzz}, $K_{B\theta_x\theta_x}$, $K_{B\theta_y\theta_y}$, $K_{By\theta_x}$, $K_{Bx\theta_y}$, K_{Bxz}, and $K_{Bx\theta_y}$. Note that the translational stiffnesses K_{Bxx}, K_{Byy}, and K_{Bzz} are highly sensitive to the axial preload which is quantified by the mean axial displacement. Thus, we obtain

$$[K]_B = \begin{bmatrix} K_{Bxx} & 0 & K_{Bxz} & 0 & K_{Bx\theta_y} & 0 \\ & K_{Byy} & 0 & K_{By\theta_x} & 0 & 0 \\ & & K_{Bzz} & 0 & K_{Bz\theta_y} & 0 \\ & & & K_{B\theta_x\theta_x} & 0 & 0 \\ & \text{sym.} & & & K_{B\theta_y\theta_y} & 0 \\ & & & & & 0 \end{bmatrix} \tag{26}$$

The combined shaft-bearing stiffness matrix is derived as follows where $\langle -1 \rangle$ implies term by term inverse

$$[K]_{SB} = [[K]_S^{\langle -1 \rangle} + [K]_B^{\langle -1 \rangle}]^{\langle -1 \rangle} = \begin{bmatrix} K_{xx} & 0 & 0 & 0 & K_{x\theta_y} & 0 \\ & K_{yy} & 0 & K_{y\theta_x} & 0 & 0 \\ & & K_{zz} & 0 & 0 & 0 \\ & & & K_{\theta_x\theta_x} & 0 & 0 \\ & \text{sym.} & & & K_{\theta_y\theta_y} & 0 \\ & & & & & 0 \end{bmatrix} \tag{27}$$

The restoring forces due to the shaft/bearing stiffness cause forces and moments at the centers of pinion and gear. Consider the two springs at both ends of the pinion shaft, their corresponding forces on the pinion are as follows, where j is the bearing index

$$\sum_{j=1}^{2} F_{SB,p,j} = \begin{Bmatrix} -K_{xx,p1}(u_{xp} + l_{p1}\theta_{yp}) - K_{x\theta_y,p1}\theta_{yp} - K_{xx,p2}(u_{xp} - l_{p2}\theta_{yp}) - K_{x\theta_y,p2}\theta_{yp} \\ -K_{yy,p1}(u_{yp} - l_{p1}\theta_{xp}) - K_{y\theta_x,p1}\theta_{xp} - K_{yy,p2}(u_{yp} + l_{p2}\theta_{xp}) - K_{y\theta_x,p2}\theta_{xp} \\ -K_{zz,p1}u_{zp} - K_{zz,p2}u_{zp} \end{Bmatrix} \tag{28}$$

The moments due to these bearing forces on the pinion are given as

$$\sum_{j=1}^{2} M_{SB,p,j} = \begin{Bmatrix} l_{p1}K_{yy,p1}(u_{yp} - l_{p1}\theta_{xp}) + l_{p1}K_{y\theta_x,p1}\theta_{xp} + l_{p2}K_{yy,p2}(u_{yp} + l_{p2}\theta_{xp}) + l_{p2}K_{y\theta_x,p2}\theta_{xp} \\ -l_{p1}K_{xx,p1}(u_{xp} + l_{p1}\theta_{yp}) - l_{p1}K_{x\theta_y,p1}\theta_{yp} - l_{p2}K_{xx,p2}(u_{xp} - l_{p2}\theta_{yp}) - l_{p2}K_{x\theta_y,p2}\theta_{yp} \\ 0 \end{Bmatrix} \tag{29}$$

Similarly, the forces and moments due to the two bearings on the gear are

$$\sum_{j=1}^{2} F_{SB,g,j} = \begin{Bmatrix} -K_{xx,g1}(u_{xg} + l_{g1}\theta_{yg}) - K_{x\theta_y,g1}\theta_{yg} - K_{xx,g2}(u_{xg} - l_{g2}\theta_{yg}) - K_{x\theta_y,g2}\theta_{yg} \\ -K_{yy,g1}(u_{yg} - l_{g1}\theta_{xg}) - K_{y\theta_x,g1}\theta_{xg} - K_{yy,g2}(u_{yg} + l_{g2}\theta_{xg}) - l_{g2}K_{x\theta_y,g2}\theta_{yg} \\ -K_{zz,g1}u_{zg} - K_{zz,g2}u_{zg} \end{Bmatrix} \tag{30}$$

$$\sum_{j=1}^{2} M_{SB,g,j} = \begin{Bmatrix} l_{g1}K_{yy,g1}(u_{yg} - l_{g1}\theta_{xg}) + l_{g1}K_{y\theta_x,g1}\theta_{xg} + l_{g2}K_{yy,g2}(u_{yg} + l_{g2}\theta_{xg}) + l_{g2}K_{y\theta_x,g2}\theta_{xg} \\ -l_{g1}K_{xx,g1}(u_{xg} + l_{p1}\theta_{yg}) - l_{p1}K_{x\theta_y,p1}\theta_{yp} - l_{g2}K_{xx,g2}(u_{xg} - l_{g2}\theta_{yg}) - l_{g2}K_{x\theta_y,g2}\theta_{yg} \\ 0 \end{Bmatrix} \tag{31}$$

5 12-DOF Helical-Gear Pair Model

First, the viscous damping matrix is derived from the modal properties of the components by assuming modal damping ratios. In the 12-DOF model, the nominal external load is treated as excitations and the parametric excitations of tooth stiffness variation and friction effects are incorporated into a time-varying K matrix. Thus, a direct implementation of modal damping ratio will result in complex-valued viscous damping terms. Consequently, only the diagonal viscous damping terms (in the damping matrix) correspond to the directions of motions are considered, i.e., the diagonal viscous damping terms are assumed to be dominant over other coupling terms. More specifically:

1. For the translational DOFs along x-, y-, and z-axes, the mesh damping force on pinion is

$$\sum_{j=1}^{2} F_{V,p,j} = \begin{Bmatrix} -2(\zeta_{xx,p1}\sqrt{K_{xx,p1}m_p} + \zeta_{xx,p2}\sqrt{K_{xx,p2}m_p}) \cdot \dot{u}_{xp} \\ -2(\zeta_{yy,p1}\sqrt{K_{yy,p1}m_p} + \zeta_{yy,p2}\sqrt{K_{yy,p2}m_p}) \cdot \dot{u}_{yp} \\ -2(\zeta_{zz,p1}\sqrt{K_{zz,p1}m_p} + \zeta_{zz,p2}\sqrt{K_{zz,p2}m_p}) \cdot \dot{u}_{zp} \end{Bmatrix} \tag{32}$$

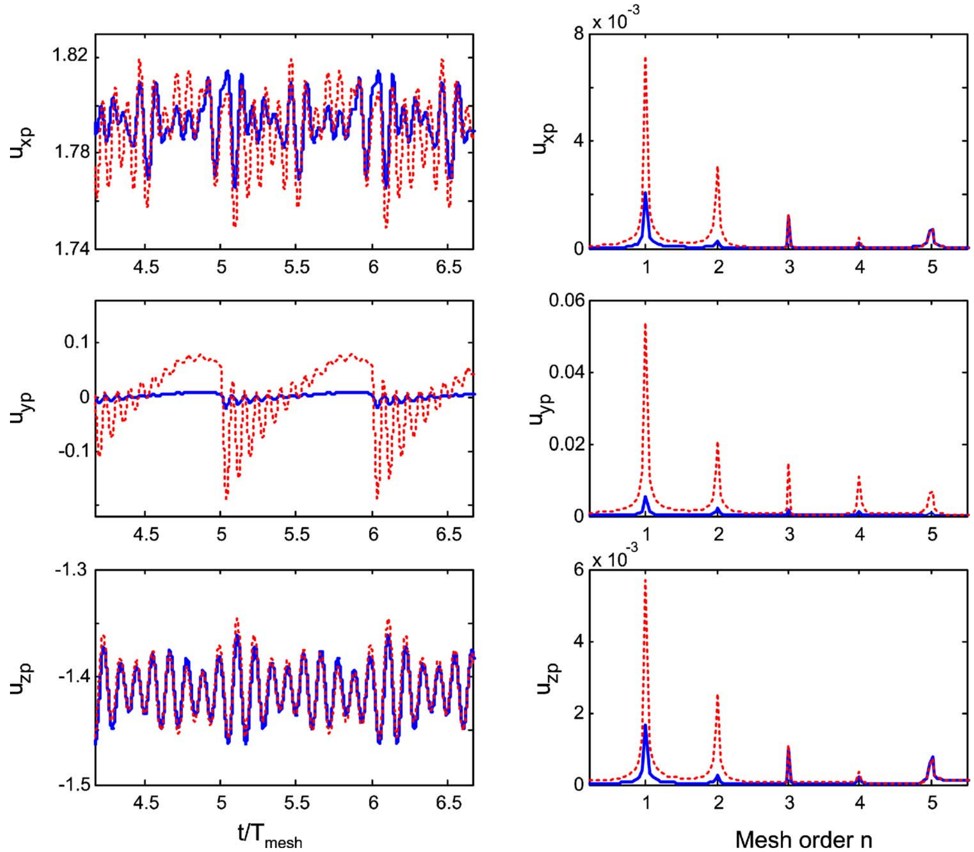

Fig. 6 Time and frequency domain responses of translational pinion displacements u_{xp}, u_{yp}, u_{zp} at T_p=2000 lb/in. and Ω_p=1000 rpm. All displacements are normalized with respect to 39.37 μin. (1 μm). Key: blue solid line μ=0.01, red dotted line μ=0.1.

The mesh damping force on the gear is

$$\sum_{j}^{2} F_{V,g,j} = \begin{Bmatrix} -2(\zeta_{xx,g1}\sqrt{K_{xx,g1}m_g} + \zeta_{xx,g2}\sqrt{K_{xx,g2}m_g}) \cdot \dot{u}_{xg} \\ -2(\zeta_{yy,g1}\sqrt{K_{yy,g1}m_g} + \zeta_{yy,g2}\sqrt{K_{yy,g2}m_g}) \cdot \dot{u}_{yg} \\ -2(\zeta_{zz,g1}\sqrt{K_{zz,g1}m_g} + \zeta_{zz,g2}\sqrt{K_{zz,g2}m_g}) \cdot \dot{u}_{zg} \end{Bmatrix} \tag{33}$$

2. For the rotational DOFs along the x and y directions (rocking motions), the mesh damping moments for the pinion and gear are:

$$M_{V,\theta_x p} = -2\zeta_{\theta_x\theta_x,p}\sqrt{K_{\theta_x\theta_x,p}J_{xp}} \cdot \dot{\theta}_{xp} \tag{34a}$$

$$M_{V,\theta_y p} = -2\zeta_{\theta_y\theta_y,p}\sqrt{K_{\theta_y\theta_y,p}J_{yp}} \cdot \dot{\theta}_{yp} \tag{34b}$$

$$M_{V,\theta_x g} = -2\zeta_{\theta_x\theta_x,g}\sqrt{K_{\theta_x\theta_x,g}J_{xg}} \cdot \dot{\theta}_{xg} \tag{35a}$$

$$M_{V,\theta_y g} = -2\zeta_{\theta_y\theta_y,g}\sqrt{K_{\theta_y\theta_y,g}J_{yg}} \cdot \dot{\theta}_{yg} \tag{35b}$$

3. For the rotational DOFs along the axial directions, the time-varying tooth mesh damping is dominant. Thus the damping moments are:

$$M_{V,\theta_z p} = -2\zeta_{\theta_z p}\sqrt{J_{zp}/r_{bp}\sum_{i=0}^{n=\mathrm{floor}(\sigma)} K_{\mathrm{mesh},\theta_z p,i}(t) \cdot (r_{rp}\dot{\theta}_{zp} + r_{bg}\dot{\theta}_{zg})} \tag{36}$$

$$M_{V,\theta_z g} = -2\zeta_{\theta_z g}\sqrt{J_{zp}/r_{bg}\sum_{i=0}^{n=\mathrm{floor}(\sigma)} K_{\mathrm{mesh},\theta_z g,i}(t) \cdot (r_{rp}\dot{\theta}_{zp} + r_{bg}\dot{\theta}_{zg})} \tag{37}$$

where i is the index for contact tooth pairs and the *floor* function rounds the contact ratio σ to the nearest integer toward minus infinity. Here, $r_{rp}\dot{\theta}_{zp}+r_{bg}\dot{\theta}_{zg}$ is the relative dynamic velocity along the LOA direction; $K_{\mathrm{mesh},\theta_z p}(t)$ and $K_{\mathrm{mesh},\theta_z g}(t)$ are the time-varying dynamic tooth stiffness functions derived earlier but considering only the rotational DOF in the z direction, and they also incorporate the effect of sliding friction.

The equations of motion for the 12-DOF helical gear pair model are derived as follows. The pinion equations in the three translational directions are

$$m_p\ddot{u}_{xp} = \sum_{i=0}^{n=\mathrm{floor}(\sigma)} F_{\mathrm{mesh},xp,i} + \sum_{j=1}^{2} F_{SB,xp,j} + \sum_{j=1}^{2} F_{V,xp,j} \tag{38a}$$

$$m_p\ddot{u}_{yp} = \sum_{i=0}^{n=\mathrm{floor}(\sigma)} F_{\mathrm{mesh},yp,i} + \sum_{j=1}^{2} F_{SB,yp,j} + \sum_{j=1}^{2} F_{V,yp,j} \tag{38b}$$

$$m_p\ddot{u}_{zp} = \sum_{i=0}^{n=\mathrm{floor}(\sigma)} F_{\mathrm{mesh},zp,i} + \sum_{j=1}^{2} F_{SB,zp,j} + \sum_{j=1}^{2} F_{V,zp,j} \tag{38c}$$

The pinion equations in the three rotational directions along x, y, and z axes are

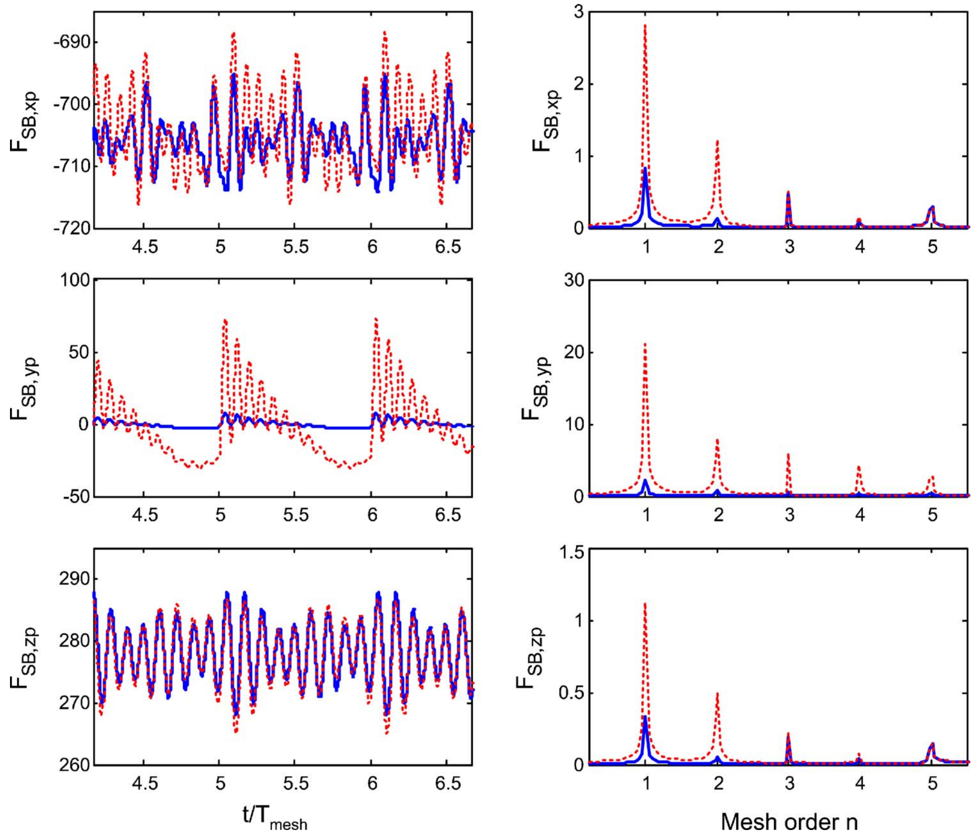

Fig. 7 Time and frequency domain responses of pinion bearing forces $F_{SB,xp}$, $F_{SB,yp}$, and $F_{SB,zp}$ at T_p=2000 lb/in and Ω_p=1000 rpm. All forces are normalized with respect to 1 lbf. Key: blue solid line μ=0.01, red dotted line μ=0.1.

$$J_{xp}\ddot{\theta}_{xp} = \sum_{i=0}^{n=\mathrm{floor}(\sigma)} M_{\mathrm{mesh},\theta_x p,i} + \sum_{j=1}^{2} M_{SB,\theta_x p,j} + M_{V,\theta_x p} \quad (39a)$$

$$J_{yp}\ddot{\theta}_{yp} = \sum_{i=0}^{n=\mathrm{floor}(\sigma)} M_{\mathrm{mesh},\theta_y p,i} + \sum_{j=1}^{2} M_{SB,\theta_y p,j} + M_{V,\theta_y p} \quad (39b)$$

$$J_{zp}\ddot{\theta}_{zp} = \sum_{i=0}^{n=\mathrm{floor}(\sigma)} M_{\mathrm{mesh},\theta_z p,i} + M_{V,\theta_z p} + T_p \quad (39c)$$

The gear equations in the three translational directions are

$$m_g\ddot{u}_{xg} = \sum_{i=0}^{n=\mathrm{floor}(\sigma)} F_{\mathrm{mesh},xg,i} + \sum_{j=1}^{2} F_{SB,xg,j} + \sum_{j=1}^{2} F_{V,xg,j} \quad (40a)$$

$$m_g\ddot{u}_{yg} = \sum_{i=0}^{n=\mathrm{floor}(\sigma)} F_{\mathrm{mesh},yg,i} + \sum_{j=1}^{2} F_{SB,yg,j} + \sum_{j=1}^{2} F_{V,yg,j} \quad (40b)$$

$$m_p\ddot{u}_{zg} = \sum_{i=0}^{n=\mathrm{floor}(\sigma)} F_{\mathrm{mesh},zg,i} + \sum_{j=1}^{2} F_{SB,zg,j} + \sum_{j=1}^{2} F_{V,zg,j} \quad (40c)$$

And, finally the gear equations in the three rotational directions along x-, y-, and z-axes are

$$J_{xg}\ddot{\theta}_{xg} = \sum_{i=0}^{n=\mathrm{floor}(\sigma)} M_{\mathrm{mesh},\theta_x g,i} + \sum_{j=1}^{2} M_{SB,\theta_x g,j} + M_{V,\theta_x g} \quad (41a)$$

$$J_{yg}\ddot{\theta}_{yg} = \sum_{i=0}^{n=\mathrm{floor}(\sigma)} M_{\mathrm{mesh},\theta_y g,i} + \sum_{j=1}^{2} M_{SB,\theta_y g,j} + M_{V,\theta_y g} \quad (41b)$$

$$J_{zg}\ddot{\theta}_{zg} = \sum_{i=0}^{n=\mathrm{floor}(\sigma)} M_{\mathrm{mesh},\theta_z g,i} + M_{V,\theta_z g} - T_g \quad (41c)$$

6 Role of Sliding Friction Illustrated by an Example

The governing equations are numerically solved for the example case. We will examine the following variables for parametric studies: (i) translational displacements u_{xp}, u_{yp}, u_{zp}, u_{xg}, u_{yg}, u_{zg}; (ii) composite displacements $\delta_z = r_{bp}\theta_{zp} + r_{bg}\theta_{zg} + u_{xp} - u_{xg}$, $\delta_y = r_{bp}\theta_{yp} + r_{bg}\theta_{yg} + u_{zp} - u_{zg}$, and $\delta_x = r_{bp}\theta_{xp} + r_{bg}\theta_{xg} + u_{zp} - u_{zg}$, which are the coupled torsional-translational motions; and (iii) dynamic bearing forces for the simplified case with $l_{p1} = l_{p2}$, $K_{xx,p1} = K_{xx,p2} = 0.5K_{xx,p}$, $K_{yy,p1} = K_{yy,p2} = 0.5K_{yy,p}$, and $K_{zz,p1} = K_{zz,p2} = 0.5K_{zz,p}$. The combined bearing force in the LOA direction for the pinion is $F_{SB,xp} = -K_{xx,p}u_{xp} - 2\zeta_{xp}\sqrt{K_{xx,p}m_p}$. Other bearing forces are defined similarly. The role of sliding friction is illustrated in Fig. 6 by comparing normalized time and frequency domain responses of u_{xp}, u_{yp}, u_{zp} (at T_p=2000 lb/in. and Ω_p=1000 rpm) for μ=0.01 and μ=0.1. Note that time t is normalized with respect to the mesh period T_{mesh}, and n is the harmonic number of the gear mesh frequency. Observe that the OLOA vibratory motion u_{yp} is most significantly affect by the sliding friction. Increasing μ almost proportionally enhances the magnitude of u_{yp} over the entire frequency range. It is consistent with Eq. (8), which shows the magnitude of the friction force is proportional to μ. The sliding friction has a moderate influence on u_{xp} in the LOA direction. An

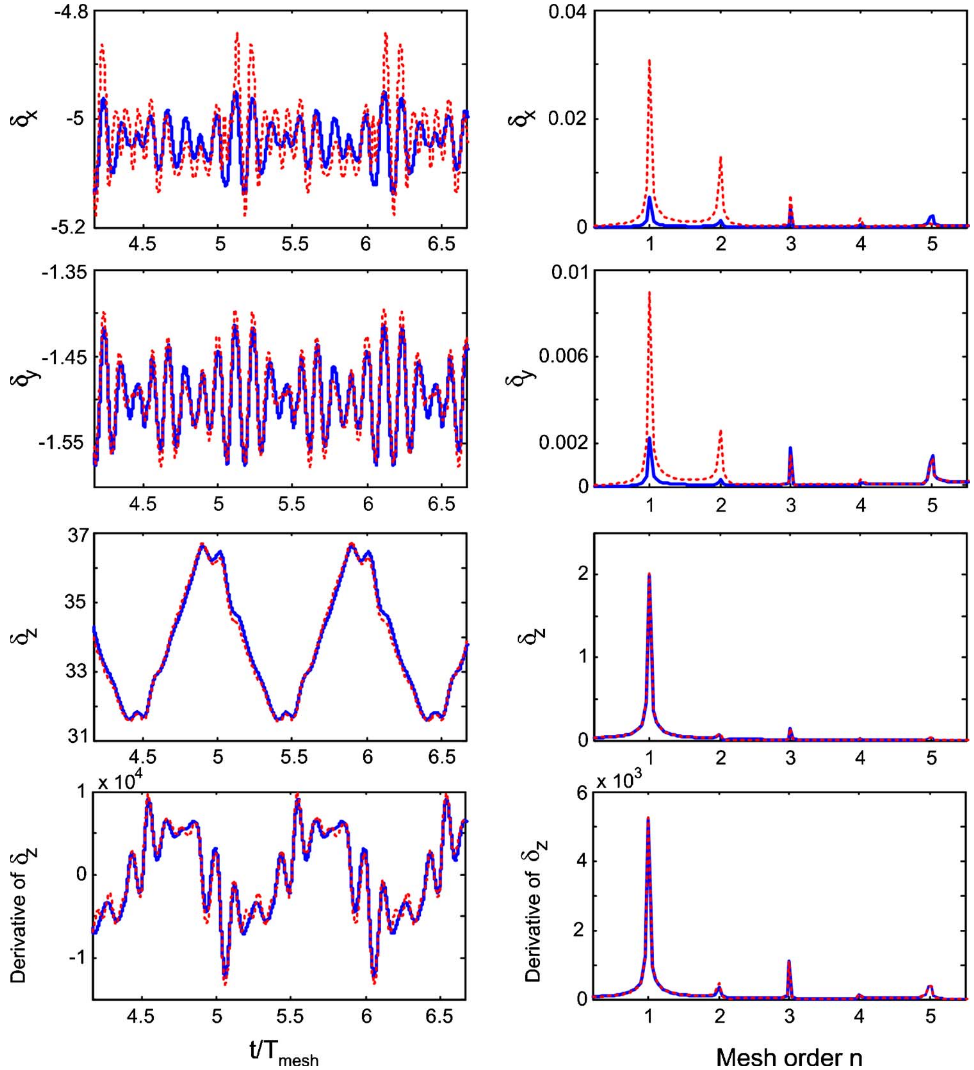

Fig. 8 Time and frequency domain responses of composite displacements δ_x, δ_y, δ_z, and velocity $\dot{\delta}_z$ at T_p=2000 lbf/in. and Ω_p=1000 rpm. All motions are normalized with respect to 39.37 μin. (1 μm) or 39.37 μin./s (1 μm/s). Key: blue solid line μ=0.01, red dotted line μ =0.1.

increase in μ significantly increases the amplitudes at $n=1$ and 2, but the higher harmonics remain almost unchanged. The axial displacements u_{xp} are least sensitive to μ except for the first two harmonics. Nevertheless, Eq. (15) shows that the axial shuttling excitation is proportional to sin β_b. Hence, it is implied that larger helical angle β_b will lead to increased shuttling excitations due to the time-varying mesh stiffness. The bearing resonances are around $n=8$ to 10, and they could be easily tuned by varying bearing stiffness. Predicted gear displacements u_{xg}, u_{yg}, u_{zg} share essentially the characteristics of pinion motions.

Figure 7 shows dynamic bearing forces in the x, y, and z directions for the pinion. Characteristics similar to the displacement responses of Fig. 6 are observed, implying that the elastic force components dominate over the viscous forces (with 5% damping ratios). Compared to the spur gear set [7], the bearing forces in the helical gear pair are reduced by more than one order of magnitude due to the gradual approach and recess motions. Figure 8 shows the composite displacements δ_x, δ_y, δ_z around the x-, y-, and z-axes. Observe that an increase in μ significantly increases the amplitudes at $n=1$ and 2 for δ_z And δ_y, but has only minor influence on δ_z. This observation is consistent with the results reported by Velex and Cahouet [4]. Nevertheless, one has to note that the amplitude of δ_z is higher than those of δ_x and δ_y by at least two orders of magnitude. To examine the effect of sliding friction, Fig. 8 also shows the time and frequency domain responses of $\dot{\delta}_z$, which is the relative torsional-translational velocity along the LOA direction. It is seen that an increase in μ introduces additional oscillations when tooth pairs pass across the pitch line. Despite that the first mesh harmonic dominates the spectral contents of δ_z or $\dot{\delta}_z$, a careful comparative study shows that the second harmonic is most significantly amplified due to friction.

The effect of sliding friction could be better observed by varying μ from 0 to 0.3 and then by generating the spectral contents of u_{xp}, u_{yp}, u_{zp}, u_{xg}, u_{yg}, u_{zg} and δ_x, δ_y, δ_z up to 15 harmonics (n) of the gear mesh frequency [18–22]. Though the resultant figures are not included here due to space constraints, some observations are as follows:

1. In the LOA direction, an in increase in μ significantly enhances amplitudes not only at $n=1$ and 2 of u_{xp} and u_{xg} (due to the reversal of friction force at pitch point), but also at higher harmonics as well, say around the torsional-transverse mode. This implies that friction force acts as a

potential source in the LOA direction to excite resonances that are controlled due to shaft/bearing compliances.

2. In the OLOA direction, an increase in μ efficiently increases the amplitudes of u_{yp} and u_{yg} over the entire frequency range, especially at $n=1$ and 2 and at the torsional-transverse resonance. This clearly shows that the OLOA dynamics are most significantly dictated by the friction effect.
3. The axial vibratory u_{zp} and u_{zg} motions are high at the torsional-transverse resonance (controlled by the axial bearing stiffness), but the resonant amplitude does not seem to depend much on μ. Nonetheless, friction significantly increases the amplitudes at $n=1$ and 2. This indicates that the shuttling forces are relatively insensitive to the sliding friction when compared with the LOA and OLOA dynamics.
4. For the composite torsional-transverse displacements δ_x and δ_y, an increase in μ increases most harmonic amplitudes, especially at the first two harmonics and at higher bearing stiffness controlled resonances.
5. An increase in μ has negligible influence on δ_z except at the second mesh harmonic. This observation is similar to that found in a spur gear pair, as we recently reported in [7]. However, the δ_z amplitude in the helical gear pair is not as significantly influenced by the sliding friction.

7 Conclusion

A new 12-DOF model for helical gears with sliding friction has been developed; it includes rotational motions, translations along the LOA and OLOA directions and axial shuttling motions. Key contributions include the following. A three-dimensional model has been proposed that characterizes the contact plane dynamics and captures the reversal at the pitch line due to sliding friction. Calculation of the contact forces and moments is illustrated by using a sample helical gear pair. A refined method is also suggested to estimate the tooth stiffness density function along the contact lines by using the FE/CM analysis [11]. Among the 12 DOFs described above, the rotational (rocking) motions around the LOA and OLOA directions and the axial motions are usually relatively insignificant. Therefore, a simplified 6-DOF model (with coordinates u_{xp}, u_{yp}, u_{xg}, u_{yg}, θ_{zp}, and θ_{zg}) similar to the spur gear model we reported in [7] could be easily derived based on Eqs. (3)–(40) by neglecting the u_{zp}, u_{zg}, θ_{xp}, θ_{xg}, θ_{yp}, and θ_{yg} variables. Such a 6-DOF model requires less computational efforts though it should yield results comparable to those by the 12-DOF model. Future work should also include validation of the proposed theory, say by running the FE/CM code in the dynamic mode and by conducting analogous experiments on gears with different friction conditions.

Acknowledgment

We gratefully acknowledge support from the U.S. Army Research Office (Grant No. DAAD19-02-1-0334 with Dr. G. L. Anderson as the project monitor).

References

[1] Vaishya, M., and Singh, R., 2003, “Strategies for Modeling Friction in Gear Dynamics,” ASME J. Mech. Des., **125**, pp. 383–393.
[2] Vaishya, M., and Singh, R., 2001, “Analysis of Periodically Varying Gear Mesh Systems With Coulomb Friction Using Floquet Theory,” J. Sound Vib., **243**(3), pp. 525–545.
[3] Vaishya, M., and Singh, R., 2001, “Sliding Friction-Induced Non-Linearity and Parametric Effects in Gear Dynamics,” J. Sound Vib., **248**(4), pp. 671–694.
[4] Velex, P., and Cahouet, V., 2000, “Experimental and Numerical Investigations on the Influence of Tooth Friction in Spur and Helical Gear Dynamics,” *Proc. ASME 2000 DET Conf.*, ASME, New York, ASME Paper No. PTG-14430, pp. 591–600.
[5] Velex, P., and Sainsot, P., 2002, “An Analytical Study of Tooth Friction Excitations in Spur and Helical Gears,” Mech. Mach. Theory, **37**, pp. 641–658.
[6] Lundvall, O., Strömberg, N., and Klarbring, A., 2004, “A Flexible Multi-Body Approach for Frictional Contact in Spur Gears,” J. Sound Vib., **278**(3), pp. 479–499.
[7] He, S., Gunda, R., and Singh, R., 2005, “Effect of Sliding Friction on the Dynamics of Spur Gear Pair With Realistic Time-Varying Stiffness,” J. Sound Vib. (in press).
[8] Borner, J., and Houser, D. R., 1996, “Friction and Bending Moments as Gear Noise Excitations,” SAE Trans., **105**(6), pp. 1669–1676.
[9] Houser, D. R., Vaishya, M., and Sorenson, J. D., 2001, “Vibro-Acoustic Effects of Friction in Gears: An Experimental Investigation,” SAE Paper No. 2001-01-1516.
[10] Blankenship, G. W., and Singh, R., 1995, “A New Gear Mesh Interface Dynamic Model to Predict Multi-Dimensional Force Coupling and Excitation,” Mech. Mach. Theory, **30**(1), pp. 43–57.
[11] ANSOL, 2003, *Helical3D User’s Manual*, Helical3D (CALYX software), ANSOL Inc., Hilliard, OH.
[12] Padmanabhan, C., Barlow, R. C., Rook, T. E., and Singh, R., 1995, “Computational Issues Associated With Gear Rattle Analysis,” ASME J. Mech. Des., **117**, pp. 185–192.
[13] Perret-Liaudet, J., and Sabot, J, 1992, “Dynamics of a Truck Gearbox,” *Proc. of 5th Int. Power Transmission and Gearing Conf.*, ASME, New York, Vol. 43, pp. 249–258.
[14] Houser, D. R., and Singh, R., 2004-05, “Basic and Advanced Gear Noise Short Courses,” The Ohio State University.
[15] Lim, T. C., and Singh, R., 1991, “Vibration Transmission Through Rolling Element Bearings. Part II: System Studies,” J. Sound Vib., **139**(2), pp. 201–225.
[16] Vinayak, H., Singh, R., and Padmanabhan, C., 1995, “Linear Dynamic Analysis of Multi-Mesh Transmissions Containing External, Rigid Gears,” J. Sound Vib., **185**(1), pp. 1–32.
[17] Lim, T. C., and Singh, R., 1990, “Vibration Transmission Through Rolling Element Bearings. Part I: Bearing Stiffness Formulation,” J. Sound Vib., **139**(2), 179–199.
[18] Singh, R., 2005, “Dynamic Analysis of Sliding Friction in Rotorcraft Geared Systems,” Tech. Report submitted to the Army Research Office, Grant No. DAAD19-02-1-0334.
[19] Umeyama, M., Kato, M., and Inoue, K., 1998, “Effects of Gear Dimensions and Tooth Surface Modifications on the Loaded Transmission Error of a Helical Gear Pair,” ASME J. Mech. Des., **120**, pp. 119–125.
[20] Guilbault, R., Gosselin, C., and Cloutier, L., 2005, “Express Model for Load Sharing and Stress Analysis in Helical Gears,” ASME J. Mech. Des., **127**(6), pp. 1161–1172.
[21] Guingand, M., de Vaujany, J. P., and Icard, Y., 2004, “Fast Three-Dimensional Quasi-Static Analysis of Helical Gears Using the Finite Prism Method,” ASME J. Mech. Des., **126**(6), pp. 1082–1088.
[22] Gagnon, P., Gosselin, C., and Cloutier, L., 1996, “Analysis of Spur, Helical and Straight Level Gear Teeth Deflection by the Finite Strip Method,” ASME J. Mech. Des., **119**(4), pp. 421–426.